Modern Physics Letters B
Vol. 26, No. 5 (2012) 1130003 (32 pages)

DOI: 10.1142/S0217984911300031

World Scientific
www.worldscientific.com

BIOPHYSICAL APPLICATIONS OF SCANNING ION CONDUCTANCE MICROSCOPY (SICM)

FRANKLIN ANARIBA* and JOON HYUNG ANH†
Department of Materials Science and Engineering, Nanyang Technological University, Block N4.1, #01-30, 50 Nanyang Avenue, Singapore 639798
**fanariba@ntu.edu.sg*
† ahnj0001@e.ntu.edu.sg

GOO-EUN JUNG
Research & Development Center, Park Systems Corp, Suwon 443-270, Korea
superdisk@parkafm.co.kr

NAM-JOON CHO
Department of Materials Science and Engineering, Nanyang Technological University, Block N4.1, #01-30, 50 Nanyang Avenue, Singapore 639798
njcho@ntu.edu.sg

SANG-JOON CHO‡
Research & Development Center, Park Systems Corp, Suwon 443-270, Korea
msjcho@parkafm.co.kr

Received 17 December 2011
Revised 16 January 2012

Scanning probe microscopy (SPM) techniques represent one of the most promising approaches to probe the physical and chemical properties of nanoscale materials. The growing convergence of physics and biology has demanded nanotechnology tools to understand the fundamental physics of biological systems. Despite the advantages of SPM techniques, there have been challenges with its application to characterization of biological specimens. In recent times, the development of one class of SPM technique, scanning ion conductance microscopy (SICM), has overcome these limitations and enabled noninvasive, nanoscale investigation of live cells. In this review article, we present the theory behind the SICM operating principles and data modeling. Based on this framework, we discuss recent research advances where the SICM technique has proven technically superior. SICM applications discussed herein include imaging of cell topography, monitoring of live cell dynamics, mechanical stimulation of live cells, and surface patterning. Additional findings on the combination of SICM with other SPM techniques as well as patch clamp electrophysiology are presented in the context of building integrated knowledge on the structure and function of live cells. In summary, SICM bridges physics and biology to enable a range of important biomedical applications.

Keywords: Ion conductance microscopy, live cell, noninvasive, biophysical applications, imaging.

‡Corresponding author.

1. Introduction

1.1. *Scanning probe microscopy (SPM)*

Nearly three decades after the introduction of the first scanning probe microscopy (SPM) technique called scanning tunneling microscopy (STM),[1–4] and twenty-five years since the introduction of atomic force microscopy (AFM), SPM techniques are some of the most common and important analytical tools in the field of surface science and materials characterization. The popularity of SPM techniques is based on their superb high resolution, ease of implementation, and the possibility to survey various phenomena (i.e., chemical, magnetic, capacitance, thermal, and current) by readily interchanging appropriate probes with minor electronic adjustments. In addition, SPM techniques have also been used for molecular engineering endeavors, especially in bottom-up molecular assembly and surface patterning.

The fundamental principle of all SPM techniques is the use of the interaction between a probe and the surface of a sample to map local physical properties. A map of the sample is built by sweeping the probe across its surface, and scanning line by line with a piezoelectric actuator or scanner. The scanner should ideally be able to control the relative position of the probe to within the resolution limit imposed by the interaction. During the rastering process, the probe-sample interaction is recorded directly or, more commonly, a feedback loop keeps one parameter (i.e., volts) at a setpoint by varying the probe-sample distance. The voltage correction to the distance is then used to form a topographical image of the substrate.

With a range of SPM techniques now available and widely utilized, each technique is mainly defined based on the specific phenomena being detected. For example, scanning tunneling microscopy (STM)[2] works by measuring a weak electrical current that flows between a sample and a very sharp metal wire tip that is used as a probe, exploiting an effect known as "tunneling," which is a quantum mechanical effect whereby electrons penetrate through an energy barrier.[5] Atomic force microscopy (AFM) is capable of individual atom resolution on both conducting and insulating surfaces while employing a force-sensitive cantilever stylus that is scanned in a raster pattern over the surface sample. The force interacting between the sample surface and the tip causes minute deflections in the position of the cantilever, which can be detected by an optical detection system.[6] Near-field scanning optical microscope (NSOM)[7] strongly relies on scanning a subwavelength aperture on a substrate which is held at a closer distance than the wavelength of radiation. Evanescent waves penetrate through the aperture and interact with the substrate.[5] The wavelength of radiation and aperture size are critical in determining image resolution, which in some instances can reach down to 20 nm.[8] Each technique has its own particular imaging capabilities, advantages and disadvantages related to its application, that largely depend on the sample of interest. Table 1 presents a list of selected SPM techniques and their measuring interactions, all of which are variants of either STM or AFM.

Table 1. List of selected SPM techniques and their measurement properties.

SPM technique	Acronym/variant	Measuring interaction	Remarks
Ballistic electron emission microscopy[9]	BEEM/STM	Electron current	Unfeasible for imaging biological samples
Chemical force microscopy[10]	CFM/AFM	Van der Waals interactions	Complex tip preparation
Conductive atomic force microscopy[11]	C-AFM/AFM	Current–voltage curves	Used on conductive and semiconducting surfaces
Electrochemical scanning tunneling microscopy[12]	ECSTM/STM	Redox reactions	Used in electroplating and batteries
Electrostatic force microscopy[13]	EFM/AFM	Electrostatic force	Sample can be immersed in solution
Magnetic force microscopy[14]	MFM/AFM	Magnetic interactions	Used on magnetic samples
Photothermal microscopy[15]	PTM/AFM	Infrared Fourier transform	Poor image resolution
Scanning electrochemical microscopy[16]	SECM/AFM	Electrochemical activity	Poor image resolution
Scanning capacitance microscopy[17]	SCM/AFM	Capacitance between probe and sample	Requires a conducting surface
Scanning ion conductance microscopy[18]	SICM/AFM	Ion conductance just above sample	Feasible for imaging live cells in solution

1.2. *Shortcomings of SPM methods in imaging biological samples*

In recent times, the increasing integration of physics and biology has demanded the introduction of tools capable of probing the physics of biological systems in a noninvasively manner. Within the framework of real-time investigation of live cells in solution, most SPM techniques possess intrinsic shortcomings. Scanning tunneling microscopy confronts several challenges for imaging live cells: First, biological samples have low conductivities and, secondly, it is nontrivial to reliably place the sample on a flat conducting surface, rendering it far from the noninvasive method needed to image live cell processes. Finally, the quantum mechanical effect of tunneling is well understood in a vacuum, but not under solution conditions.

In the case of the AFM, there are three traditional imaging configurations: contact mode, tapping mode, and noncontact mode. In the invasive contact mode, the sharp tip is dragged along the substrate commonly damaging soft biological tissue, as shown by Henderson *et al.*[19] and You *et al.*[20] In the less intrusive tapping mode, the tip oscillates at amplitudes above 100 nm causing the tip to intermittently contact the sample, which can damage soft biological tissue. In the noninvasive noncontact mode, the tip does not contact the sample and sample imaging mostly relies on van der Waals interactions between the tip and the surface. Since the tip is usually oscillating above its resonant frequency at amplitudes of less than

Table 2. Capabilities of several SPM techniques in characterizing living cells.

SPM technique	Sample	Imaging of live cells	Image resolution	Damage to sample
STM	Conducting	No	—	—
AFM	Conducting and insulating	Yes	High	Yes
NSOM	Conducting and insulating	Yes	Poor	No
SICM	Conducting and insulating	Yes	High	No

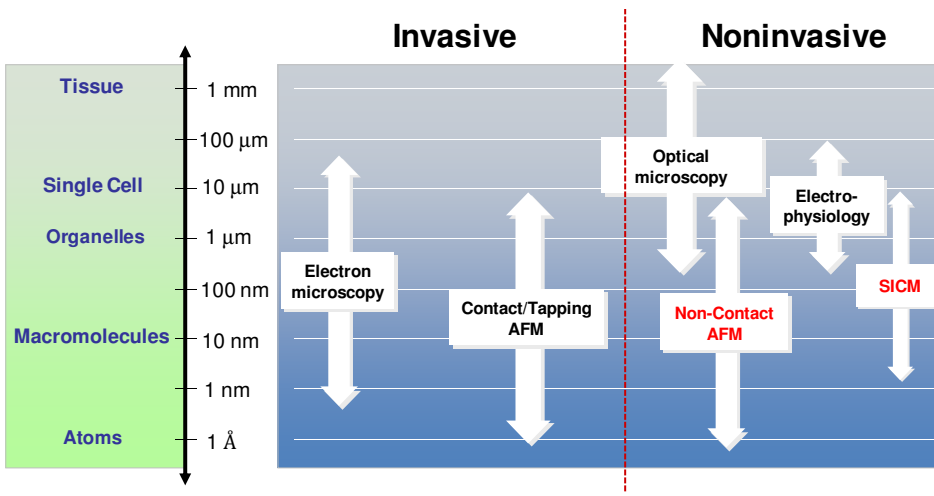

Fig. 1. Depiction of various SPM techniques currently used to characterize biological specimens in an invasive and noninvasive manner. The scale on the left indicates the image resolution of the techniques. Notice that noncontact AFM and SICM are two techniques available for the high resolution imaging of live cells.

10 nm, the tip has a tendency to "stick" to biological samples, making the imaging process a rather difficult endeavor. In addition, for both noncontact and tapping modes, imaging of live cells is carried out under solution conditions, which convolutes data interpretation due to perturbations and artifacts introduced by the liquid environment.

As for NSOM, in general, the technique provides poor image resolution when the sample is under solution due to shortcomings in controlling the distance between the near-field aperture and the sample under solution conditions.[8] Table 2 summarizes the clear advantages of scanning ion conductance microscopy (SICM) for characterizing live cells under physiological conditions over more widely use SPM techniques, such as STM, AFM, and NSOM.

Figure 1 depicts various SPM techniques currently available to characterize biological specimens in an invasive and noninvasive manner. Noncontact AFM and SICM are two analytical tools available for studying biological samples noninvasively. However, scanning ion conductance microscopy (SICM) is a more promising

technique than noncontact AFM, for it is capable of providing reliable, truly non-invasive, high resolution topographical images of both soft biological samples and live cells.

1.3. *Scanning ion conductance microscopy: A promising bioimaging technique*

1.3.1. *Principle and composition*

Scanning ion conductance microscopy (SICM) was first developed by Hansma *et al.* in 1989.[18] Unlike other SPM techniques, SICM was designed specifically to probe biological systems by providing information about the topography of soft nonconducting samples, such as cell membranes under physiological conditions. The measurement principle of SICM is based on monitoring changes in ion conductance between two electrodes. Figure 2 displays a schematic view of a SICM system.

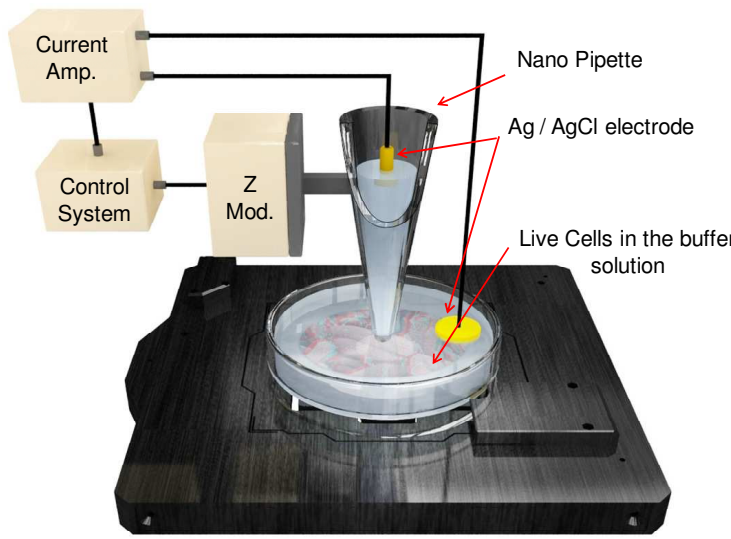

Fig. 2. Schematic view of a SICM system, depicting the nanopipette, Ag/AgCl electrodes, current amplifier, control system, and piezoelectric element (Z mod).

In general, SICM employs a glass nanopipette filled with electrolytic solution as a probe, and the sample to be analyzed is placed in a reservoir of electrolytic solution. There are two electrodes, one inside the nanopipette and another in the reservoir solution. An applied bias is then introduced between the two-electrode electrochemical cell. The nanopipette is then lowered towards the sample while the ion conductance between an electrode inside the nanopipette and another electrode located in the reservoir solution is observed. The position of the nanopipette tip in relation to the surface strongly affects the observed ion conductance between

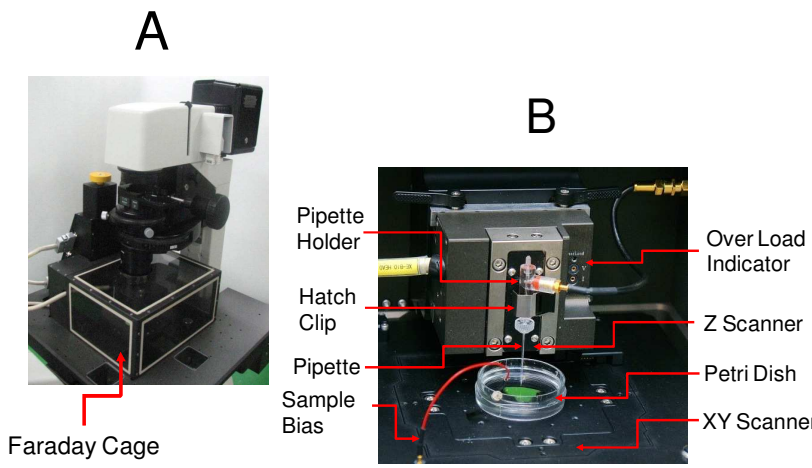

Fig. 3. (A) Complete SICM system including a Faraday cage. (B) Description of a scanning head for a SICM instrument (XE-Bio from Park Systems Corp.).

the two electrodes. As the nanopipette tip is brought closer to the surface of the sample, the space through which ions flow is minimized, causing the ionic current between the two electrodes to decrease. Subsequently, the nanopipette is scanned in a rastering manner across the surface while a feedback loop adjusts the vertical position to keep the ion conductance constant by either lowering or raising the nanopipette tip, enabling the topography of the surface to be mapped with very high resolution.[18] Figure 3(A) shows a SICM platform containing a Faraday cage to protect against environmental, static and electromagnetic interference. Panel (B) in Fig. 3 depicts the various mechanical parts of a SICM instrument head, including the Z and XY scanners, pipette, hatch clip, and pipette holder.

1.3.2. *Modes of operation*

There are three main scanning modes of SICM operation: Direct current (DC) mode, alternating current (AC) mode, and hopping mode, also known as Approach-Retract Scan (ARS) and backstep mode. Figure 4 depicts the various operational modes of SICM. Figure 4(A) depicts the DC mode while Fig. 4(B) shows a schematic of the AC mode. Figure 4(C) illustrates the working mechanism of the hopping mode, whereby the current drift, prevalent in DC and AC modes, is nullified, allowing for the imaging of live cells in solution at high resolution over long periods of time.

In DC mode, the nanopipette is scanned laterally over the contours of the surface by maintaining the ionic current through the nanopipette tip at a constant value through continuous adjustments of the z-axis. In DC mode, the ionic current monitored is greater farther away from the surface, but decreases as the nanopipette approaches the surface of the sample, greatly diminishing the sensitivity of the tech-

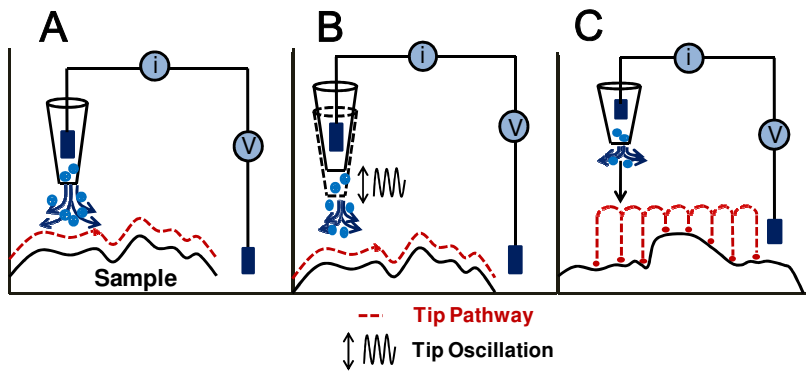

Fig. 4. Three operational modes of SICM. (A) Direct current (DC) mode. (B) Alternating current (AC) mode, and (C) Hopping mode (also known as Approach-Retract Scan (ARS) or backstep mode).

nique. In addition, the image resolution is highly dependent on the diameter of the nanopipette, providing a classical resolution of approximately 200 nm.[18] According to Shevchuk *et al.*[21] one nanopipette tip radius distance from the surface of the sample is desirable because such distance provides the most successful image resolution. In addition, DC mode can suffer from loss of feedback control when the value of measured current has varied 0.2–3% from its initial setpoint. This usually occurs while scanning over long periods of time. Furthermore, DC mode is highly susceptible to electrode drift (i.e. current instabilities and electronic noise), further limiting the effectiveness of the technique. However, Mann *et al.*[22] reported some improvement in controlling the electrode drift by establishing a pulse mode of height controls. The procedure consisted in the application of a test pulse with the intention of eliminating some of the drift due to temperature fluctuations.

In AC mode, the height of the nanopipette with regards to the surface is modulated in the z-direction in order to generate a standing modulated current wave (I_{mod}) that is present in the overall current. The modulated current is used to provide the signal for the feedback mechanism controlling the height of the nanopipette. Furthermore, Imod is highly sensitive when the nanopipette is near the surface, and even more so as the probe approaches the surface. Likewise, as in DC mode, the image resolution is also dependent on the overall size of the nanopipette, and with the appropriate gain controls, the precision in position control can be as high as 2 nm.[21,22] Overall, the AC mode offers a series of advantages over AC mode including:

(i) high sensitivity,
(ii) minimal electrode drift, and
(iii) real-time monitoring at higher resolution.

In general, the AC mode provides superior results than DC mode when utilized on flat samples. However, both operational modes are prone to collision with steep features on contoured samples.

Both above-mentioned SICM operational modes are based on a continuous feedback, but in hopping mode a different reference current point is set each time a measurement is acquired. Briefly, at each imaging point, the nanopipette is directed towards the sample from a starting position farther up from any surface feature. While the nanopipette is away from the surface, a reference current is set. Subsequently, the nanopipette is lowered towards the sample until a specific predetermined value (i.e. until the current is reduced to less than one percent). When the current reaches that set point, the height of the nanopipette is recorded. Finally, the nanopipette is pulled back up and moved laterally to a new setpoint. Then, the cycle starts again, all the while the probe never gets in contact with the sample.[23] The x, y, z-coordinates can then be stored for a later reconstruction of the surface topography.[24] This technique circumvents the disadvantages associated with DC and AC modes by offering high resolution images of uneven samples, and therefore nonconvoluted images of cell body, axon and dendrites.

One disadvantage of hopping mode is the long acquisition time in comparison to regular scanning DC and AC operational modes. To accelerate the image acquisition process, a series of software steps can be implemented:

(i) The entire image can be subdivided into equal areas (i.e. squares, and the overall roughness of the area estimated by measuring the height difference at each corner). If the mean roughness is high, then a high resolution image can be acquired. On the other hand, if the mean roughness of the area is low, the area can be imaged at low resolution.
(ii) The amplitude of the nanopipette withdrawal can be adjusted to move up just above the pre-determined roughness of each sample area, hence saving time since the nanopipette need not pulled all the way up.

Overall, in hopping mode a low resolution image can first be taken to identify a feature of particular interest which can be later imaged at higher resolution. As a result, the speed of the image acquisition is fast enough to image live cells in spite of movements associated with rearrangement and migration of the cells. Taken together, the current 7 drift due to electrode fouling and associated with DC and AC modes is eliminated in hopping mode while at the same time providing high resolution, noninvasive images of contoured biosamples.[23,25,26]

Although the various operational SICM modes vary according to implementation, all rely on monitoring the ion current between the electrode inside of the nanopipette and the electrode in the reservoir solution. Hence, it is of fundamental importance the complete understanding of factors affecting the monitored ionic current. These factors have been thoroughly addressed through various important theoretical studies, some of which are present below.

2. Theoretical Modeling of SICM

Theoretical modeling of the resistance or ionic current observed in SICM derives from earlier semi-analytical modeling carried out in the Allen Bard group during the introduction of the scanning electrochemical microscopy (SECM)[16] and subsequent work by Nitz and coworkers,[27] in which a mathematical model is presented to describe the relationship between observed ionic currents and tip-sample distances when a nanopipette approaches a planar surface. In brief, the full analytical model separates the overall resistance into three components: resistance of the nanopipette (R_p), a distance dependent resistance (R_z), and the resistance of the electrolyte solution outside the nanopipette radius (R_r). In general terms, the resistance of the nanopipette is given by Eq. (1):

$$R_p = \frac{1}{k}\frac{h}{\pi r_e r_i}\,, \tag{1}$$

where h is the nanopipette height; k is the conductance of the electrolyte solution; r_i is the inner radius of the nanopipette opening, and r_e is the radius of external electrode. The overall observed ion current as a function of tip sample distance dependence along the z-axis can be approximated by Eq. (2):

$$I_{\mathrm{DC}} \approx I_{\mathrm{sat}}\left(1 + \frac{3/2\ln(r_o/r_i)r_e r_i}{dh}\right)^{-1} \tag{2}$$

where r_o is the outer radius of the nanopipette, d is the nanopipette tip to sample separation, and I_{sat} is given as:

$$I_{\mathrm{sat}} = \frac{V}{R_p} \tag{3}$$

where V is the applied votage.[27,28] Pastré *et al.*[29] approximated the decrease of observed ionic current in a conical shape nanopipette as a function of tip-sample distance (z-axis):

$$I_{\mathrm{DC}} \approx I_{\mathrm{sat}}\left(1 + \frac{3\ln(r_o/r_i)r_i r_o}{3dL}\right)^{-1}, \tag{4}$$

where L is the distance between the electrode and the nanopipette opening. Close examination of Eqs. (2) and (4) reveals differences in the approximations, most likely the result of differences in the mathematical approach. When the SICM instrument is operated in alternating current (AC) mode, the amplitude of the modulated current as a function of tip-distance (z-axis) is given by Eq. (5):

$$I_{\mathrm{AC}} = \int_0^T I_{\mathrm{DC}}(d + a\sin[2\pi ft))\sin(2\pi ft)dt] \tag{5}$$

where T is the modulation period, f is the modulation frequency, I_{DC} is the current due to the DC component, and a is the modulation amplitude of the AC component.[29] A plot of observed I_{DC} and I_{AC} versus tip-sample distance (z-axis) reveals that the DC component decreases monotonically, while the AC component

displays a sharper decline. For instance, experimental data indicates that when the nanopipette is 30 nm away from the surface, the slope of the AC approach curve is three times more sensitive than that of the DC approach curve. This observation is reasonable considering that the AC approach curve is similar to the first derivative of the DC approach curve.[29]

Edwards *et al.*[28] also presented a detailed 2D simulation when the nanopipette is perpendicular to a planar surface using finite element modeling (FEM). The current was calculated by integrating the flux on the boundary of the electrode, Ω:

$$\pi = 2\pi k \int_{\Omega} r \cdot \nabla V \cdot \mathbf{n}\,, \tag{6}$$

where $\mathbf{n}$ is the unit normal to the edge, V is the potential, and ∇V is related to the equation given below:

$$\nabla^2 V = \frac{\partial^2 V}{\partial r^2} + \frac{1}{r}\frac{\partial V}{\partial r} + \frac{\partial^2 V}{\partial z^2} = 0\,, \tag{7}$$

where r and z are the radial and axial components in the cylindrical polar coordinate system. In order to simplify the solution, the authors made a series of assumptions: The electrolyte conductivity, k, and the potential V are set to unity. The solution is calculated by solving Eq. (8):

$$i = \int_0^{2\pi} \int_0^{\gamma} \left(- \frac{\beta}{r_o 2} \right) k r_o 2 \sin\varphi d\varphi d\theta\,, \tag{8}$$

where γ is the semiangle of the conical section of nanopipette and $\varphi < \gamma$ and both are portions within the bounds of the nanopipette in the 2D cylindrically symmetric simulation, and β is given below:

$$\beta = \frac{r_o r_i}{r_i - r_o}\,, \tag{9}$$

where r_i is the inner radius of the nanopipette and r_o is the outer radius of the nanopipette. Upon integration of Eq. (8), the current is given by Eq. (10):

$$i = 2\pi\beta(1 - \cos\gamma)\,. \tag{10}$$

In addition, the authors also carried out 3D simulations to study the effects of various nanopipette geometries, including for a tip above a planar surface, a tip near a step edge, and a tip over a cylindrical pit. The equation used to calculate the observed ionic current is analogous to Eq. (6):

$$i = 2k \int_{\Omega} r \cdot \nabla V \cdot \mathbf{n}\,, \tag{11}$$

where Ω represents the boundary surface of the electrode. The novelty of the FED simulations was the introduction of the nanopipette angle of approach as an important variable.

C.-C. Chen and L. Baker[30] noticed that previous theoretical studies lacked complementary experimental data to support the validity of the presented mathematical

models. As a result, the authors further developed the ability to quantify the measurements of localized conductance, through experiments and models, by examining ion current profiles and the effects of probe-sample distance with SICM. Specifically, their theoretical model affords to provide additional information in relation to ion currents in regions of nonuniformed electrolyte conductance around a nanopore in a porous membrane by adopting a disk shape as the source of ions, instead of the standard hemispherical geometry. The magnitude of the ion currents recorded with SICM is given by the total resistance between the electrode inside the nanopipette and the electrode located on the opposite side of the porous membrane. This way, the total resistance (R_T) is the sum of nanopipette resistance (R_p), the access resistance (R_{AC}) and the membrane resistance (R_m). The nanopipette resistance is approximated by Eq. (12):

$$R_p \cong \frac{\omega \cot\left(\frac{\theta}{2}\right)}{\pi r_i}, \tag{12}$$

where ω is the specific resistance of the electrolyte inside the nanopipette, θ is the cone angle of the nanopipette tip and r_i is the radius of the nanopipette tip opening. The access resistance is represented by Eq. (13):

$$R_{\mathrm{AC}} \approx \frac{3/2 \ln\left(\frac{r_o}{r_i}\right)}{k\pi d}, \tag{13}$$

where r_o and r_i are the outer and inner radius of the nanopipette opening, k is the electrolyte conductivity and d is the probe-sample separation. The resistance of the membrane is described by Eq. (14):

$$R_m = \left(\frac{1}{k'N}\right)\left(\frac{l}{\pi b2} + \frac{1}{2b}\right), \tag{14}$$

where k is the electrolyte conductivity within the pore of the membrane, l is the membrane thickness, b is the radius of the pore opening, and N is the number of cylindrical pores in the membrane. However, the membrane resistance is negligible in comparison to R_p and R_{AC}, hence R_T is given by only these two terms. The overall current magnitude is estimated by Eq. (15):

$$I = \frac{V}{R_T} = \frac{V}{R_p + R_{\mathrm{AC}}}, \tag{15}$$

where V is the applied voltage. For further considerations, such as the dependence of R_{AC} on the local conductivity established by the ion flux emanating for the pore, and the validation of the mathematical modeling, the reader is referred to Ref. 30 in this review.

In another study, Rheinlaender and Schffer[31] also used FEM to investigate the image resolution and formation process, specifically the height measurements of small particles on a planar surface, and discern particle image resolution. They defined lateral resolution of SICM as the smallest distance at which two small particles

can be clearly resolved from each other in an image. Such a distance is reported to be $3r_i$, or three times the inner radius of the nanopipette tip opening. In addition, the authors also calculated that particles with a lateral width below approximately $6r_i$ will display heights that are only a fraction of the actual magnitude, and that for two low particles close in distance to each other the image can appear rotated by 90°. Taken together, factors affecting image resolution need to be taken into considerations accordingly.

3. Factors Influencing Image Resolution of SICM

There are several influential factors of particular interest involved in higher resolution imaging that are worth mentioning. The first factor of interest is the nanopipette size. In studies carried by Korchev *et al.*[32] it was demonstrated through experimental current-distance curves that nanopipettes fabricated with smaller tip radius display higher sensitivity. In other words, employing finer nanopipettes means surveying the surface at a closer distance, which implies higher resolution imaging, especially when operating SICM in AC mode. For instance, a nanopipette of a diameter smaller than 20 nm leads to an image resolution in the order of less than 30 nm.

A second factor in determining the image resolution is the working distance of the probe to the surface. For DC mode whereby the current drops when the probe approaches the surface, it has been calculated that the optimum distance corresponds to a value of $0.2r_i$ for a nanopipette angle of approach of 3°, where r_i is the inner radius of the nanopipette.[31] The effect of the angle of the nanopipette on the surface is another important factor determining the image resolution. Edwards *et al.*[28] calculated that increasing the angle over a flat surface resulted in a steeper drop of sensitivity as the probe approached the surface. The authors calculated probe sensitivity for angles of 3°, 5°, 10°, and 15° and explained the results in terms of the internal resistance of the nanopipette as a function of a large constant resistance in series, whereby the larger the resistance of the probe, the smaller the resistance outside the nanopipette. That is to say, it is advantageous to increase the angle of approach of the nanopipette to reduce its resistance contribution, hence increasing overall sensitivity of the probe close to the surface of the sample.[28,31] This phenomenon is even more pronounced in AC mode.[28] Finally, the effect of increasing the ratio of the outer nanopipette radius to the inner nanopipette radius ($R = r_o/r_i$) has a similar effect as increasing the nanopipette angle of approach to the surface. However, the drop in observed ionic current with decreasing tip-sample distance is a more significant factor than utilizing nanopipettes with larger R values or increasing angle of approach of the probe.[28]

All of the above-mentioned factors contribute to the overall observed current. In a more simplified version, the current observed can be explained in terms of Ohms law, whereby the overall resistance in series is a contribution of the resistance of the nanopipette plus the ionic resistance in the bath solution. Ohms law can then

be expressed as in Eq. (16):

$$l = \frac{V}{R_p} + \frac{V}{R_d}\,, \tag{16}$$

where V is the applied bias, R_p is the nanopipette resistance, and R_d is the ionic resistance along the path from the reservoir solution to the tip opening. R_d depends on the distance between the probe and the sample, geometry of sample, and electrochemical properties of the surface.[33]

It is important to note that live cells undergo constant cellular activity at the cell surface, which may affect the electrolytic local concentration. This can have an impact in the image resolution by affecting height detection. In other words, cellular equilibrium dynamics can affect the dimensions of observed features. Happel and Dietzel[24] calculated the time required for cells to reach local equilibrium. In brief, let us assume the conductance of the electrolytic solution is controlled by sodium chloride, with a concentration given by C_o and a diffusion coefficient in water at room temperature of $\sim 10^{-9}$ m^2/s. Next, at the interface of the sample surface we assume an area depleted of sodium chloride given by a cube with edge length of $l = 1$. Defining the coordinate $x = 0$ as the position of the interface between the cube (located at $x > 0$) and the reservoir solution at $x < 0$ in one dimension, Ficks second law describes the sodium chloride diffusion into the cube, and so the average concentration at location x inside the cube at time t is given the following differential equation:

$$C(t) = \frac{1}{l}\int_0^l c(x,t)dx\,, \tag{17}$$

where $c(x,t)$ is the concentration at position x at time t. To solve the equation the authors make a series of assumptions with regard to the concentration inside and outside the cube. At $t = 0$ sec, $c = 0$ mM inside the cube, and outside the cube $c = C_o$. For locations far away and $t > 0$, the same boundaries conditions apply, $c = 0$ mM, and $c = C_o$. The solution yields Eq. (18) shown below:

$$C(t) = \frac{\sqrt{Dt}}{\pi} \cdot \frac{C_o}{l} \tag{18}$$

which upon further simplification results in $C(t = 0.001 \text{ sec}) = C_o$, or about 10 msec. The authors concluded that cellular concentration changes occur about 60 times less than the time required to acquire an image using SICM, thus demonstrating that the technique affords imaging live cells without compromising on resolution.

4. Applications of SICM

Recently, SICM has been applied to answer fundamental questions in important areas of cell biology. Specifically, the technique affords imaging live cells with high resolution without causing any damage to the sample, and capturing cell activity

by monitoring membrane dynamics in real time. In addition, the probe can be used to stimulate cell activity and capture the various cell responses. Moreover, the nanopipette is also capable of serving as a delivery vehicle for drug administration. All of the above-mentioned techniques are covered in some detail below.

4.1. *Noninvasive topographical imaging of live cells*

Further SICM applications in the noninvasive imaging of stem cells[34–36] and living cardiovascular cells[36] have previously been summarized. One of the first applications of SICM in the biological field was reported by the Yuri Korchev group. In one study, they successfully imaged live cells of the type of murine melanocyte line melan-b because they are small, flat and dendritic, ideal for SICM investigation in DC and AC modes. The acquired SICM images provided a full plethora of common features usually observed in melanocytes. These included cell alignments, nuclear areas, cell borders with short processes, longer branching processes, nonadherent adjacent cells, and possibly cell junctions. Furthermore, other observations consisted of cell contact with apparent filaments, a ruffle membrane of one cell overlapping another, and apparently processes containing specialized organelles called melanosomes.[32]

In a subsequent report, Korchev and coworker[33] demonstrated the noninvasive nature of SICM by acquiring a series of high resolution images of human colon cancer cells for a period of eight hours, during which the cell remained viable. The most important finding was that surface features on cell membranes, usually only observed by SEM after fixation and staining, were imaged through SICM. Figure 5 [Panels (A), (B), (D)–(F)] displays SICM real time images of a confluent monolayer of a human colon cancer cell line (Caco-2) in a 1:1 mixture of phosphate buffered saline and culture medium. The cell remained viable for eight hours of continuous scanning. Panels (A) and (B) illustrate movements of the "junction" between five cells. Panels (D) and (E) were taken at higher resolution and show a wide range of surface morphologies, such as filamentous architectures. Panel (F) displays numerous projections, which appear to be a developing brush border, and panel (C) represents a scanning electron micrograph of mammary carcinoma cells (Rama 25), which self-assemble in a monolayer, similar to human colon cancer cells.

In another example of advantages of SICM over AFM, analysis of the images in Fig. 5(E) shows a series of filamentous structures, which under higher magnification appeared as furrows, possibly due to the interaction between internal filaments and cell membrane. This observation contrasted with AFM studies which had shown that the filamentous structures were directed upward, most likely the result of tip-induced deformation.[33,37]

Gorelik *et al.*[38] imaged live Xenopus kidney epitheilial A6 cells. The authors listed a series of important observations gained from the SICM images. First, numerous nanoscale features were observed on the cells. In one instance a cell with sparse microvilli generating ridges was spotted and, in other images, cell changes including lateral expansions and contractions of the cell membrane and rearrange-

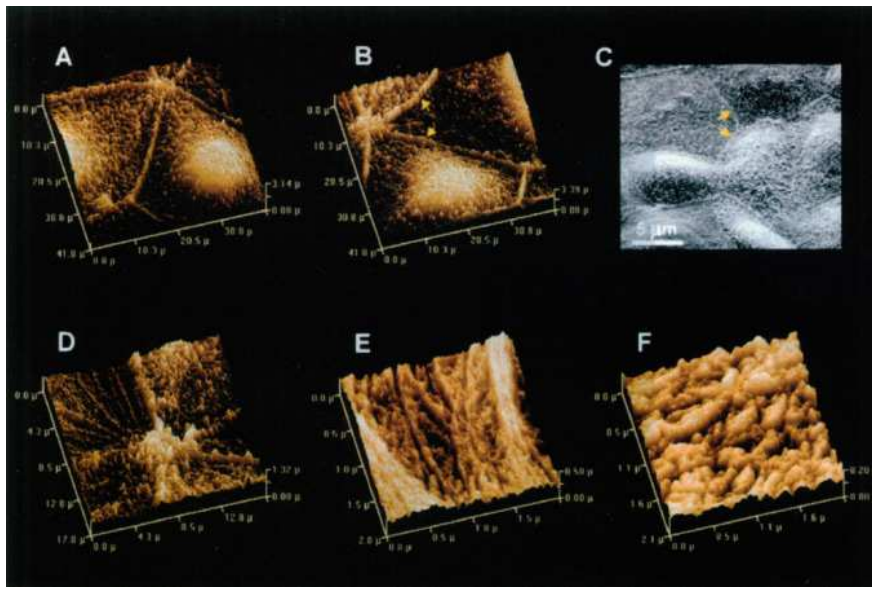

Fig. 5. Panels (A), (B), (D)–(F) are SICM real time images of a confluent monolayer of a human colon cancer cell line (Caco-2). The cells remained viable and motile during the eight hours of continuous scanning. Panels (A) and (B) exhibit images taken 140 min apart, and exemplify movements of the "junction" between five cells. (C) SEM of mammary carcinoma cells (Rama 25) in culture. Arrows in Panels (B) and (C) appear to show cell boundaries. Reprinted with permission from Ref. 33. Copyright 1997 Elsevier.

ment of the microvilli pattern were distinguished. Secondly, SICM images were acquired while the cells were viable and motile under physiological conditions, a clear advantage over scanning electron microscopy (SEM), which requires the cells to be fixed for imaging. As an example, the images taken on the fixed cells were comparable to SEM images in that both lack observable cell activity, strongly suggesting the rearrangements observed in live cell images were due to cellular activity and not a result of stimulation due to the SICM imaging process. Finally, live A6 cells grown on membrane filters were characterized for a period of 10 hours, with each scanning taking 20 min to acquire. Significant cell changes were witnessed, such as the reshaping of cell borders, and changes in cell volume and height.

In another contribution to the application of SICM, Shevchuk *et al.*[39] acquired high resolution SICM images of proteins in living cell membranes. They first calculated the resolution of the SICM instrument by imaging a monolayer of cell surface layer proteins from Bacillus Sphaericus CCM2177 on a mica surface. Concurrent scans of the same sample provided identical images, suggesting the protein layer was not degraded by the nanopipette. The resolution was calculated by taking a SICM high resolution image, computing a fast Fourier transform (FFT) on the same image, and finally applying a FFT filtering process. Since discreet spots between three and six nm rings were observed, the lateral resolution was surmised to be in the

range of 3-6 nm. This way, high resolution images of the head and anterior midpiece of a live boar spermatozoa that had undergone a spontaneous acrosome reaction in a buffer solution, revealed protrusions that appear as projecting particles. By taking two images 10 min apart on the same region, stable regions were witnessed between these two scans. Thus, the combination of high resolution imaging with the ability to repeatedly scan the same location at close time intervals is highly advantageous for the functional mapping of ion channels and the investigation of other cell dynamics.

4.2. *Investigating dynamics of live cells*

As described above, SICM can obtain topographic image of live cells, indicating that this technique is expected to be used for analyzing dynamics of live cells. Cell membrane dynamics, such as the localization of ion channels, cell movements, morphological changes, and cytoskeletal rearrangements, are vital for the overall understanding of cell function. In spite of its importance, efforts to characterize cell dynamics have been traditionally hindered by continuing challenges in imaging subcellular structures with tens of nanometer resolution of live cells. One available method has been fluorescence microscopy, but there are a series of challenges involved with this approach:

(i) Limited observation window due to photobleaching and photoinduced degradation.
(ii) Labeling is primarily done by immunostaining, which can alter ion channel function.
(iii) Nonspecific staining is problematic, and most importantly,
(iv) the majority of sample preparation for fluorescence labeling requires cell fixation.

Another potential method of use is AFM. Although it can theoretically resolve nanometer features, there is substantial damage to the cell membrane during image acquisition.[37,40–42] Mainly due to its ability to overcome the above-mentioned challenges, various SICM applications to cell dynamics, such cell movements, volume changes, structural formations, and localization of ion channels have been introduced as follows.

Happel and coworkers[43] monitored cell movements and morphological changes with a modified SICM setup, which employs both current pulses (pulse-mode, analogous to AC mode), and backstep or hopping mode. Observation of cell dynamics was accomplished by repetitive imaging of the same oligodendrocytes from the porcine corpus callosum over a range of 30 min. Cell changes were obtained by scanning the cells in a perfusion chamber while varying the osmolarity of the reservoir solution.

Zhang and coworkers[41] observed cell division by high resolution SICM. Cells for these studies were grown for 12 days until a tight epithelial monolayer was formed.

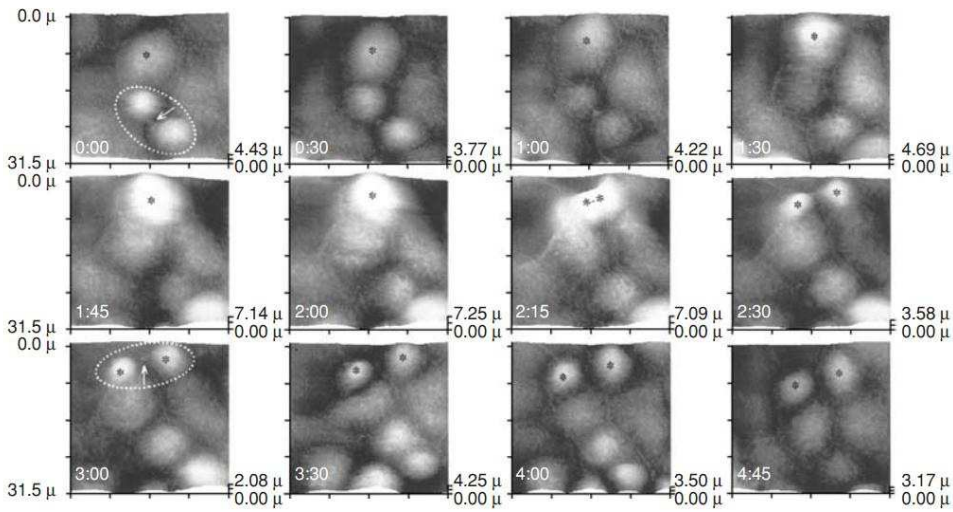

Fig. 6. Five hour time-lapse SICM observations of A6 cell division process. An A6 cell, marked by asterisk in the upper left corner Panel (0:00 hour), is undivided, but has started to show signs of cell division. Subsequent frames monitored the progress of the cell division of the asterisked cell, from 0:00 hours to 4:45 hours. Reprinted with permission from Ref. 41. Copyright 2005 Nature Publishing Group.

Time-lapse SICM images were taken for a period of five hours as shown in Fig. 6. A series of twelve images are displayed which clearly demonstrates a cell undergoing cytokinesis, a process whereby the cytoplasm divides through a cleavage procedure. Moreover, during such a cell division process, cells move relative to one another and change multicellular interactions without losing epithelial monolayer integrity.

In another study, Gorelik *et al.*[40] studied the dynamics of microvilli formation and retraction in live Xenopus kidney epithelial A6 cell line. These cells are ideal for this type of investigation because they form a monolayer with numerous microvillous structures and established tight junctions. Therefore, by employing timelapse SICM imaging for 10 hours dynamics of microvilli were consistently recorded, and only after the addition of formaldehyde to the reservoir solution, cell dynamics effectively stopped. After a wide range analysis which included human colon cancer cells (Caco-2 line), murine melanocytes (melan-b line), breast cancer cells (T47D cell line), and fibroblasts (COS-7 cell line), the authors concluded that the dynamics of microvilli are inherent to nonspecialized microvilli, regardless of their cell origin.

Gorelik *et al.*[44] used SICM imaging to examine changes of the surface structure of cell membranes in cultured ventricular cardiomyocytes after the detubulation with formamide. The authors confirmed the loss of T-tubule openings in the formamide-treated cells. The cardiomyocytes displayed increasing disorganization and loss of the T-tubule pattern as a function of time. Correspondingly, Duclohier[45] reported the identification of cardiac voltage-dependent sodium channels (VDSC) near T-tubules openings in ventricular heart cells.

Since SICM lends itself for the mapping of ion channels, Shin and Gillis[46] observed changes in the surface morphology associated with exocytosis after stimulation with high K^+ ion concentration. Stimulation of exocytosis needs membrane depolarization and extracellular Ca^{2+} ions. Using AC mode, cells were imaged before and after depolarization with a bath solution comprised of 50–70 mM K^+ ions. The results indicated that cells that undergo exocytosis after K^+ ion stimulation showed changes in membrane morphology, such as punctuated depression associated with fusion and collapse of vesicles into the surface membrane.

In a similar but important study, Korchev *et al.*[42] studied the localization of ATP-regulated K^+ ion channels in myocytes, presumably involved in governing regional specialization for precise and localized control over cell function. Results indicated that K_{ATP} channels hold their position on the cell surface for long periods of time, suggesting a connection to the cytoskeleton in the sarcolemma. Furthermore, the K^+ ion channel positions are located in the Z-grooves and the authors proposed these channels are involved in the precise, localized, and unrecognized control over the propagation of the voltage difference along the T-tubule system. The novelty of this research study was the use of the SICM nanopipette to stimulate the cell membrane via K^+ ion chemistry. Hence, utilizing the nanopipette for chemical cell stimulation can easily be extended to using the nanopipette for mechanical cellular stimulation, in such a way as to stimulate cellular mechanosensitive responses.

4.3. *Mechanical stimulation of live cells*

Mechanosensitive ion channels work by converting an external mechanical stimulus into chemical and electrical signals. Moreover, mechanosensitive ion channels presumably participate in the mechanotransduction process in the action potential generator region of sensory fibers where pressure is transduced into an electrical signal. The excitation of mechanoreceptors is achieved by opening or closing ion channels present in sensory cells. Among the various purposes of mechanosensors are determining systemic osmolarity, blood pressure, muscle stretch, and limb positions. Although mechanosensitiviy is essential for the operation of different cell functions, the underlying bases of mechanosensation remain obscure.[47–50] Hence, the mechanical stimulation of live cells provides valuable insight into the nature of the inner workings of mechanosensing. A series of approaches have been previously employed to stimulate cell reaction. For instance, magnetic twisting cytometry, patch clamp, AFM, and stimulation through micropipettes. All of these analytical tools are nonconducive to reliable and systematic mechanosensing studies. On the other hand, the nanopipette in the SICM instrument can produce a reliable, reproducible, localized, and controlled mechanical stimulation in live cells.[51]

Mechanical stimulation can appear in two forms: contact and noncontact. The contact approach involves switching off the feedback control in the SICM instrument while lowering the nanopipette vertically against the surface of the cell. The lowering of the nanopipette is controlled by a piezoelectric element to determine

distance and duration of the stimulus. The noncontact approach entails lowering in a piezo-control manner the nanopipette towards the cell membrane while applying a pressure jet of air from the tip of the nanopipette. The positive air pressure, in excess of 13 KPa, produces a jet of liquid from the tip opening.

Sanchez *et al.*[51] demonstrated that contact approach in cell stimulation is problematic, due in part to damage caused to the cell membranes by the nanopipette. The noncontact approach offers at least several clear advantages. First, it limits the cell membrane damage. Second, the stimulation is localized allowing for the study of mechanoelectric transduction phenomena within small regions, and lastly, the stimulus can be repetitively applied. The authors utilized Ca^{2+} ion imaging experiments to determine the response of DRG sensory neurons to mechanical stimulation. The responses varied according to the type of stimulation the cell received. For instance, the contact approach produced an all or none type of response, while for the noncontact approach the response was graded, and unlike the contact approach, there was a correlation between the rise of observed Ca^{2+} ion concentration and stimulus intensity. Sanchez and coworkers[52] also investigated the application of a noncontact approach to red blood cells, epithelial cells, cardiomyocytes, and neuron cells. The noncontact approach involves a SICM system in dc mode modified with a pressure port where a jet of air stimulates the cells in question, without the nanopipette ever making contact with the surface of the substrate. This way, the authors were able to apply positive and negative pressure while they examined the cell response.

Another development has been the use of SICM to guide and redirect neuronal growth cones. This was accomplished by reducing the tip-sample distance during scanning by using a threshold off five percent of current decrease. Interestingly enough, the intensity or polarity of the DC current used did not play a role in the growth induction process. Likewise, the nature of the pipette filling solution, such as culture medium, 25% diluted culture medium solution, or isotonic saline solution, did not stimulate growth. However, line scans moving away from the cone, and pipettes with inner diameters of about 600 nm were effective in producing growth of cones and even the enlargement of a lamellipodium.[53] In another similar effort, Pellegrino *et al.*[54] took advantage of weak hydrostatic forces in scanning SICM to guide neuronal growth cones, hypothesizing that applied pressure functions as a directional cue. Overall, SICM allows for the contact and noncontact localized stimulation of living cells in a systematic, reliable, reproducible, and controllable manner.

4.4. *Surface patterning*

The localized stimulation of live cells through the nanopipette can be developed into a delivery vehicle for chemicals of interest to specific sites on the cell membrane, while allowing for the cell reaction to be imaged. This is of particular interest in the development of therapeutic drugs delivery systems for both *in vivo* and *in vitro* studies. It is possible to deliver molecules in a controlled manner via the

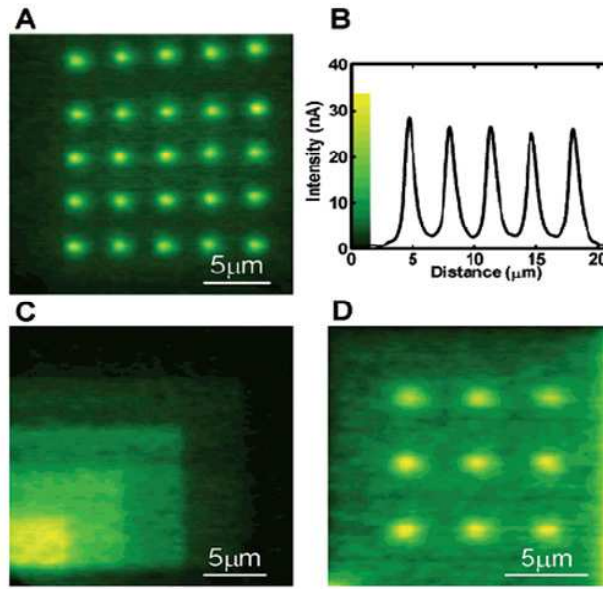

Fig. 7. (A) Fluorescence images of 25 dots of biotinylated ss-DNA deposited for 10 seconds each onto a streptavidin-coated glass surface. (B) Line scan of the bottom row in panel (A). (C) Squares of biotinylated ss-DNA, ranging from 4 μm to 17 μm, written one square over the other to create a pattern with rising intensities. (D) Dots of protein G on a positively charged glass surface. Reprinted with permission from Ref. 58. Copyright 2002 American Chemical Society.

nanopipette. The delivery through the tip opening is controlled by various factors such as electro-osmotic flow, electrophoresis, and dielectrophoresis, depending on the size, charge and polarizability of the molecules of interest. For instance, applying a negative bias to the counter electrode relative to the nanopipette produces no noticeable flow of DNA out of the tip orifice, but when setting a positive bias on the same counter electrode, molecules flow out of the tip opening and this flow has been shown to be linear with applied voltage.[55–57]

In this manner, Bruckbauer *et al.*[58] were able to deliver fluorophore labeled single-stranded DNA (ss-DNA) in a controlled manner, forming various single component fluorescent patterns on a streptavidin-coated glass substrate. The authors used the fluorescence of Rhodamine Green-labeled ss-DNA monitored by scanning confocal microscopy to observe imprinted patterns caused by the deposition of the ss-DNA on streptavadin-coated glass surfaces. The potential was kept at +0.6 V, providing a flux of molecules in the range of 4000 molecules per second. Curiously, protein G was deposited inside the nanopipette tip opening upon the application of a negative potential in the counter electrode relative to the nanopipette, which is contrary to the negative potentials used for ss-DNA deposition. Figure 7 illustrates the various patterns formed by the voltage-controlled deposition of ss-DNA and protein on a functionalized glass surface.

In a subsequent report, Bruckbauer *et al.*[59] demonstrated that goat anti-rabbit IgG antibodies and ss-DNA could be delivered from the nanopipette or "nanopen" at −0.5 V and the deposition increased linearly with applied negative potential. More importantly, the antibodies retained their biological activity even after deposition, and the deposited ss-DNA was fully functional as illustrated by hybridization studies. Finally, the authors showed that consecutive deposition of biomolecules on the same spot can be carried out, thus allowing for the creation of fluorescent patterns with controlled concentration gradients.

In another application, Bruckbauer *et al.*[60] established that SICM can also be used to carry out reactions at the tip of a glass nanopipette. The authors produced an enzymatic cleavage of fluorescein diphosphate (FDP) by confining it in volumes of 100 attoliters to the tip of the nanopipette. Subsequently, the nanopipette was immersed in a bath solution containing the enzyme alkaline phosphatase (AP). The enzyme biomolecules physisorbed onto the tip of the glass nanopipette by diffusion, and/or through the assistance of a voltage pulse. The concentration of the enzyme in the bath solution linearly correlated with the number of molecules physisorbed onto the glass tip. The subsequent confined reactions were tracked by monitoring the fluorescence via a confocal microscope. The enzymatic "nanoreactor" offers potential applications in miniaturized screening. This experiment was limited to an enzymatic assay at the tip of the glass nanopipette; however, the "nanoreactor" can easily be used to carry out reactions just above the membrane surface of live cells and other nanostructures of interest.

All of the above applications of surface patterning were undertaken under solutions conditions, which presented a challenge for nanoimprinting registry, due in part to the uncontrolled diffusion of the molecules in the liquid environment. As a result, it had been difficult to deposit two different types of molecules without significant overlap, which is in itself a requirement for the production of complex surface patterning. The introduction of the double-barreled nanopipette by Rodolfa *et al.*[61] addressed this issue. Double-barreled nanopipettes are fabricated from glass capillaries with a septum in the center, creating two compartments with a pipette puller, as shown in Fig. 8. Two types of molecules can be delivered and deposit simultaneously by fine tuning voltage-driven controls. A great advantage of the method is the deposition is carried out in air, thus providing smaller feature size, and the ability to form complex graded patterns involving two colors.

In a subsequent work, Roldolfa *et al.*[62] demonstrated the creation of a small array of water droplets by using the double-barrel nanopipette. The authors used the water droplet array to carry out biochemical reactions. For instance, the double-barrel nanopipette was used to create droplets containing fluorescein diphosphate. Then the cleaving enzyme alkaline phosphotase was added to cleave diphosphate and give a fluorescent product. In a similar manner, a linked transcription:translation kit was used to produce green fluorescent protein in the droplet array. In another application of the "nanopen", individual molecules were delivered

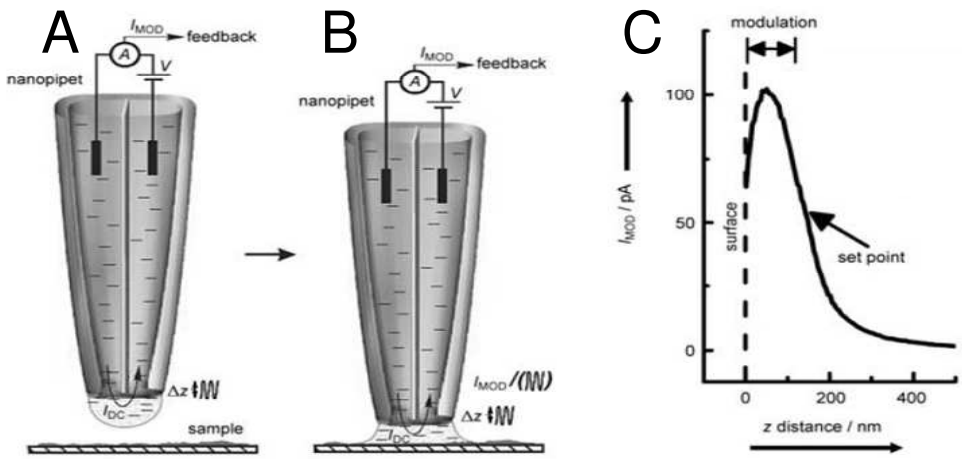

Fig. 8. Graphic representation of a double-barreled nanopipette. (A) The voltage applied between Ag/AgCl electrodes within the two barrels of a glass nanopipette creates a direct ion current (I_{DC}) in a droplet. (B) When the tip is brought into contact with a surface, modulation in the z-direction creates an alternating ion current (I_{MOD}), providing the feedback signal. (C) Approach curve for the double-barreled nanopipette acquired over a PDMS surface. It is worth mentioning the strong dependence of (I_{MOD}) to distance when close to the surface. Reprinted with permission from Ref. 61. Copyright 2005 John Wiley and Sons.

in a controlled manner to preselected sites on the plasma membrane of a live boar spermatozoa cell. The authors delivered fluorophore-labeled probes which they then monitored through single molecule fluorescence tracking, this way being able to follow the diffusion of membrane glycoproteins in various cell membrane domains.[63] Alternate methodologies to patterning proteins and peptides utilizing SICM can be found in a review article by Christman *et al.*[64]

5. In Tandem Applications of SICM

As part of the SPM family of techniques, SICM uses a versatile platform which can combine with a range of complementary techniques, including patch-clamp, scanning confocal microscopy, scanning near infrared optical microscopy, and scanning electrochemical microscopy.

5.1. *Patch-clamp*

Patch-clamp as a sensitive technique for the study of open ionic channels on cellular membranes was first reported by Neher and Sakmann back in 1976.[65] Briefly, patch-clamp is a technique of conductance measurements of open cellular ionic channels. The technique works by isolating an area of a cellular membrane from which current measurements are carried out. The isolation is possible via an extracellular glass pipette, which is closely sealed against the surface of the membrane. The ion channels in the isolated patch of membrane can be chemically stimulated

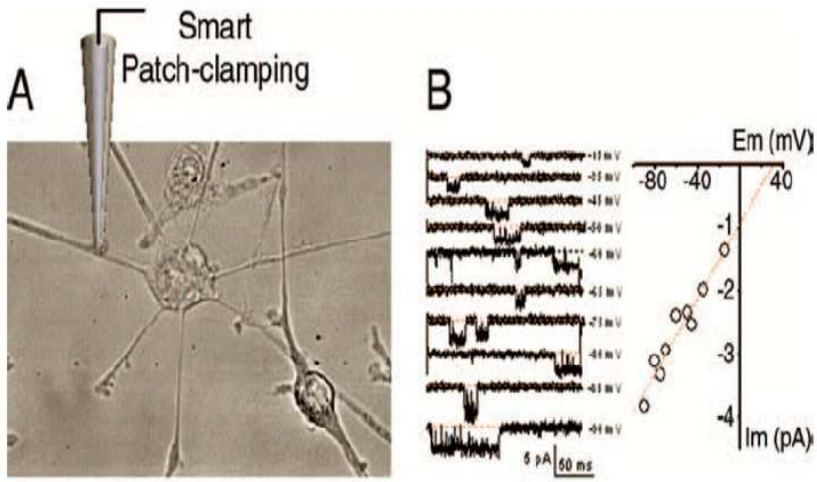

Fig. 9. Assessment of neuronal differentiation of neural crestlike stem cells using SICM. (A) Optical image of the experimental arrangement whereby the nanopipette is positioned on the dendrite of the neural crestlike stem cell. (B) Single channel recording of a Na^+-like ion channel from a pluripotent neural crestlike stem cell line. Reprinted with permission from Ref. 34. Copyright 2008 Mary Ann Liebert, Inc.

via the glass pipette. For instance, the presence of cholinergic agonist results in the recording of square pulse current waveforms when individual acetylcholine-receptor channels are stimulated. Further enhancements to patch-clamp were later implemented: For example, the correlation between tip geometry and closeness of the tip to the membrane, the ability to form a high seal resistance or low leakage current,[66] and the minimization of background electrical noise through the creation of giga-ohm seals.[67]

Scanning patch-clamp or smart patch clamp systems[38,42,68–70] are two different names given when SICM is combined with electrophysiology. Figure 9 depicts a classical SICM/patch-clamp experimental setup on stem cellderived neuron cells.

Both techniques strongly complement each other. For example, Korchev *et al.*[42] were able to use SICM imaging to obtain topographical information, such as Z-grooves of the cardiamyocyte sarcolemma. Based on the topology observed and using the x–y coordinates of the SICM instrument, the authors used patch-clamp to locate K^+ ion channels within the Z-grooves. This way, they mapped the distribution of single K_{ATP} channels in the cells interrogated, correlating topographic features with functional activity in the cardiomyocyte sarcolemma.

Similarly, ion channels of Ca^{2+} were mapped in the T-tubule regions of cardiomyocyte sarcolemma, while Cl^- ion channels were identified within the regions of T-tubule openings and Z-grooves. The spatial co-localization of Cl^-, Ca^{2+}, and K^+ ion channels in the sarcolemma region of the T-tubule system provided valuable information on the synergistic coupling between the various channels.[68] A fundamental advantage of SICM combined with patchclamp is the ability to probe small

cells and subcellular structures that otherwise are not possibly probed with patch-clamp alone, partly due to the inability to observe these features under optical microscopy: One such example are microvillous structures. Smart patch clamp can be used to study nontransparent cell samples, including brain slice samples, hair cells, and epithelial cultures. More importantly, the precision and feedback mechanism of the SICM/patch clamp in tandem arrangement unlocks the possibility for automated patch clamp with potential applications in drug screening.[68,69] In another study by Dutta *et al.*,[70] further evidence that maxi-anion channels and ATP release sites activities are correlated in neonatal rat cardiomyocytes are put forth.

In summary, the combination of both SICM imaging and patch-clamp is a powerful in tandem configuration allowing for the correlation of cell topography with cell activity, granting overall new insights into cell functionality.

5.2. *Scanning confocal microscopy*

Scanning confocal microscopy (SCM) is widely used in the biology-related fields of science as a way to visualize or measure fluorescence from biological tissue or cells. The combination of SICM and SCM was reported by Gorelik *et al.*[71] and termed scanning surface confocal microscopy (SSCM). SSCM takes advantage of the glass nanopipette commonly used in SICM to obtain topographical information of the surface and a laser, pinhole, and photosensor or camera to collect fluorescent images. The relevant point worth noticing is that the laser is focused on the tip opening of the nanopipette, thus eliminating stray light and spatially aligning topography and fluorescence.[72] The in tandem arrangement allows for the simultaneous recording of topographic and quantitative fluorescence images of the cell membrane, all in a single scan. Moreover, SSCM affords the imaging of live cells for both topography and fluorescence as a function of time. The authors summarized three significant advantages of this technique:

(i) Fluorescently-labeled particles can be directly correlated with cell structure topography.
(ii) The measurement of quantitative fluorescence information can be accomplished, and
(iii) the autofluorescence usually experience in SCM is minimized, partly due to a lower fluorescence background from the surface scan.[71]

Figure 10 displays a schematic of the SSCM configuration.

In another application, SSCM resolution was improved to the point of imaging single virus particles on cell membranes, thus opening the possibility of monitoring the entry of a virus into a cell in real time. In order to correlate topographical features with fluorescence images, the position of fluorescence spots were mapped and their location superimposed on the topographical image. The virus-like particles (VLPs) were observed on the cell membrane as topographical protrusions in correspondence to fluorescence responses.[73] Figure 11 compares scanning surface

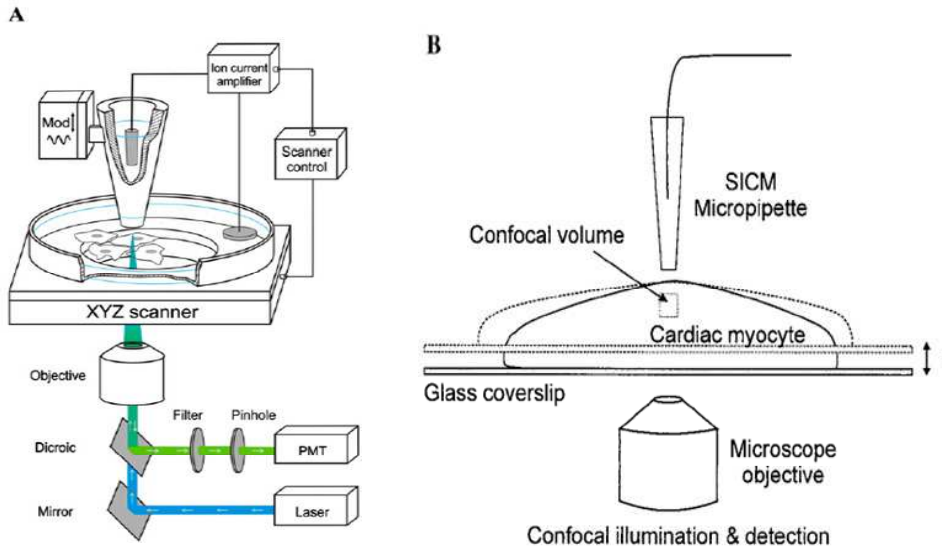

Fig. 10. (A) Schematic diagram of simultaneous SICM and laser confocal microscopy. (B) Diagram for SSCM on a contracting cardiac myocyte. When the cardiac myocyte contracts the feedback control moves the sample stage to maintain a constant distance between the nanopipette and the cell surface. The confocal volume probed, therefore, remains at the same point below the cell surface. Reprinted from permission from Refs. 21 and 73. Copyright 2008 Elsevier.

confocal microscopy and conventional confocal microscopy. Note that SSCM has the advantage of correlating topographical information with fluorescence imaging.

Shevchuk and coworkers[72] carried out studies of both fixed and live cells using SSCM. Of particular relevance was their conclusion that endocytotic pits on COS-7 cells were resolved topographically for the first time, and that 89% of the detected pits were chathrin-coated. One drawback was their SSCM scan rate was not fast enough to elucidate endocytotic pits in live cells.

5.3. *Near-field scanning optical microscopy*

Near-field scanning optical microscopy (NSOM) is sometimes called near-infrared scanning optical microscopy. In NSOM, a near-field light source with an output aperture probe of dimensions smaller than the source wavelength is scanned above the sample surface. In order to achieve high resolution images, the probe must be held in the near-field regime of the surface, at a distance much smaller than the wavelength of radiation. However, for the imaging of biological samples in liquids, it is still difficult to reliably control the sample-probe distance, one of its principal challenges for imaging biological samples. Korchev *et al.*[74] built a combined NSOM-SICM setup in order to take advantage of the latters probe-sample control mechanism. This combined setup enabled dual imaging of live cardiomyocytes, where Z lines and Z-grooves were clearly discernable. In addition, the authors suggest that

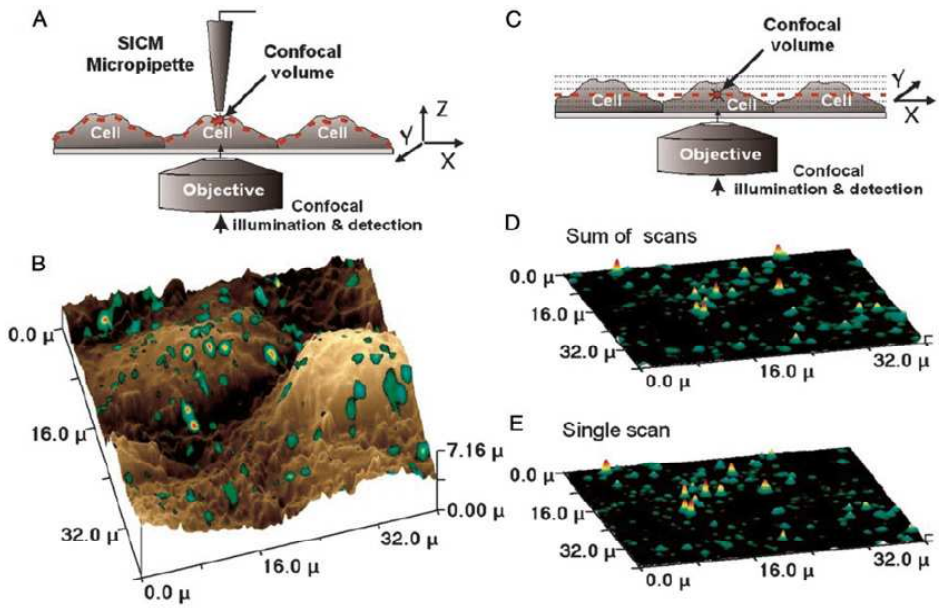

Fig. 11. Surface confocal and conventional confocal microscopy comparison. (A) SSCM configuration, whereby the dotted line indicates the position of the optical image of the cell surface acquired in a single scan. (B) Overlay of simultaneously acquired topographic and fluorescence images. (C) A conventional scanning confocal microscope configuration whereby the dotted lines represent the multiple optical cross-sections needed to generate an image. (D) Image generated by the addition of eight cross sections of the same sample as shown in panel (B). (E) Image generated by a single cross section scan of the same sample as shown in panel (B). Reprinted with persmission from Ref. 71. Copyright 2002 The National Academy of Sciences.

the decrease in light intensity which occurs when using a smaller nanopipette for higher resolution scans can be compensated by a higher numerical aperture objective and an improved photon counting setup. In a related study, Shevchuk and coworkers[21] used SICM in AC mode, coupled with NSOM, to acquire simultaneous images of cardiomyocytes. However, in this case, the Z-grooves were clearly visible on both images, but the NSOM image resolution was only modest, suggesting that the design of the combined setup is important for optimizing imaging capabilities.

In another combined SICM-NSOM study, Mannelquist *et al.*[75] utilized the higher image resolution capabilities of this setup to correlate topographical and fluorescence information of polystyrene beads adsorbed on a glass surface under liquid conditions. Given the precise control of NSOM probe-sample distance offered by this method, the authors also identified that NSOM provides higher resolution images than SICM, since the maximum laser power used under solution conditions is no longer limited to < 10 mW, as is the case under ambient conditions. Further refinements enable a direct correlation of the SICM and NSOM images, and SICM showed higher resolving power of the surface features of the observed closely-packed micron-scale beads.[76]

Rothery *et al.*[77] also assembled a hybrid SICM-NSOM instrument and imaged for the first time fixed urchin sperm flagella and calculated resolutions on the order of 220 and 190 nm for SICM and NSOM, respectively. Subsequent imaging of live A6 cells displayed a good correlation between topographical and optical data. It is worthwhile to mention that the images were acquired under physiological conditions, whereby the advantage of using a hybridized version of SICM-NSOM was strongly demonstrated.

5.4. *Scanning electrochemical microscopy (SECM)*

SECM is a valuable technique for surveying the chemical reactivity of material surfaces at microscopic scales by placing an ultramicroelectrode (UME) just above the surface of interest. The technique functions by immersing the sample and UME in an electroactive solution. When the UME is biased, a current is generated. As the UME approaches the surface, the current generated at the tip of the UME changes based on the redox activity of the surface, hence mapping the redox activity of the substrate. Generally, an amperometric mode of detection is used,[78] but later refinements have included a potentiometric detection system.[79] Another recent development has been the fabrication of borosilicate micropipettes containing a gold ring electrode with the added advantage of determining the position of the tip relative to the sample with nanometer accuracy.[80]

Takahashi and coworkers[81] fabricated and characterized a similar probe to that of Comstock *et al.*[82] (gold ring UME) to acquire simultaneous images by SECM and SICM. With this combined setup, they were also able to image deposits of Horse Radish Peroxidase enzyme that were immobilized on a glass substrate. Additionally, using the hybridized apparatus in hopping mode, they obtain topographical and electrochemical information on superior cervical ganglion, A6 live cells, and cardiomiocytes, where varicosities, veins responsible for the neuron transduction and axon formation, were clearly visualized. Furthermore, by monitoring the Faradaic current for O_2, ($K_4[Fe(CN)_6]$), and $FcCH_2OH$ on cardiomyocytes, they demonstrated for the first time the simultaneous characterization of the localized permeation property of a live cell membrane.

6. Outlook

In recent years, the SICM technique has become an increasingly versatile tool in the biological sciences, addressing a number of important questions at the level of the cellular membrane. Indeed, the membrane interface supports a wide range of biological processes including selective transport, cellular recognition, cytoskeleton anchorage, cellcell junctions, and signal transduction pathways, in addition to serving as a protective barrier and separating the biochemical activities of different cellular compartments. With the capability to study these structures and functions in a non-contact, liquid format with nanoscale resolution, there are many oppor-

tunities for the SICM technique to improve upon current measurement capabilities in the biomedical sciences.

Among the possibilities, there is great potential for characterizing the microvilli of cell surfaces, which are important for absorption, secretion, and mechanotransduction. In Fig. 12, time-lapse SICM imaging of COS-1 monkey kidney cells followed the dynamics of microvilli, establishing a platform upon which the pathology of diseases involving microvilli can be explored. Moreover, the increased presence of microvilli on the cell surface is a hallmark feature of many types of transformed cancer cells versus normal cells.[83–85]

SICM imaging is able to detect the formation of microvilli from ciliary membranes of hepatic cancer cells, as shown in Fig. 13. Unlike the AFM technique for which imaging of soft micro-projections is very difficult, SICM is uniquely able to follow the formation of these structures on live cell surfaces and may therefore play an important role in understanding cancer pathogeneses.

Another area where the SICM technique can improve functional analysis is the assessment of drug activity in live cells. The SICM pipette enables the controlled delivery of drugs to a single cell. Based on this capability, the effects of drug administration can be monitored by characterizing the changes in morphology and membrane structure which occur in the primary cell as well as nearby cells. These studies could enable early *in vitro* analysis of drug toxicity, mechanisms of action,

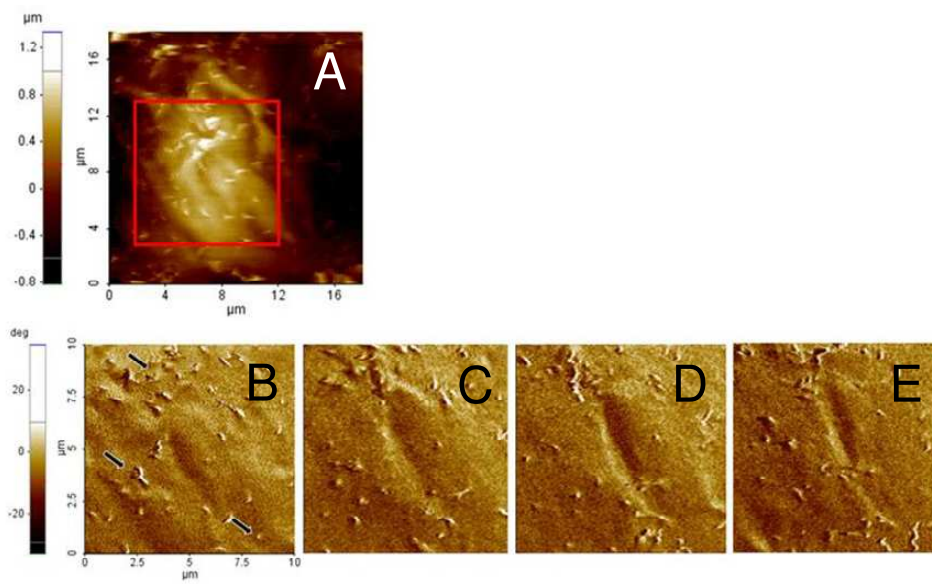

Fig. 12. SICM images of live COS-1 Monkey Kidney cells. Panel (A) is a 20 × 20 μm image of Kidney cells. Panel (B) is a 10 × 10 μm inset of panel (A). Panels (B)–(E) are 10 × 10 μm images that illustrate cell dynamics. The arrows in panel (B) indicate the dynamics of microvilli on live COS-1 cells for a period of four hours.

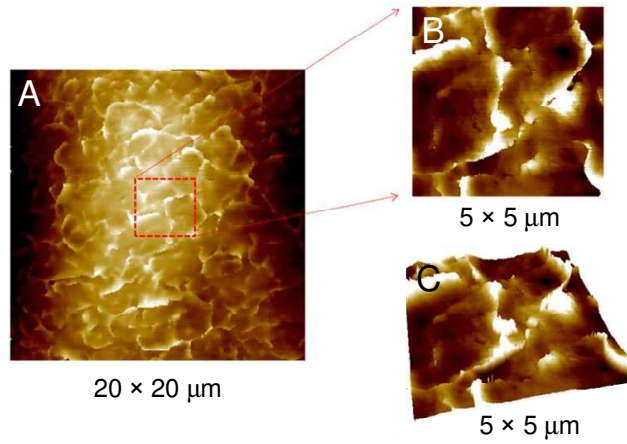

Fig. 13. (A) 20 × 20 μm SICM image of microvilli formation from ciliary membrane on surface of hepatic cancer cell under physiological conditions. (B) Depiction of 5 × 5 μm inset of panel (A) that clearly shows microvilli formation. (C) Three-dimensional image of panel (B).

and efficacy in order to reduce the time and resources required for clinical drug development.

Taken together, there are many important applications in the biomedical sciences where a balance between imaging resolution, method of sample preparation, and measurement principle must be achieved in order to functionally probe the membrane interfaces of live cells. The imaging capabilities of the SICM lend the technique significant potential to achieve this balance, and reveal physiologically relevant insights for clinical diagnosis, molecular toxicology, and pharmaceutical drug development.

To date, there has not been a widely available SICM instrument, thereby limiting the number of potential users as well as making it difficult to directly compare results obtained on different instruments. With the recent development of the XE-Bio model by Park Systems Corp., which combines AFM, SICM, and inverted optical microscopy, there is now the opportunity for a wider range of users to take advantage of the SICMs measurement capabilities, to establish a standardized framework for sample imaging and analysis, and for confirming findings within the field. In doing so, we can move beyond technology development, and towards the identification of new applications in the biomedical sciences where the SICM can answer questions intractable to current methods, and bridge the gap between the basic and clinical sciences.

Acknowledgments

We thank Tatsuo Ushiki for reading this manuscript and for his valuable comments and suggestions. We gratefully acknowledge funding support from the National Research Foundation (NRF — NRFF2011-01), and from the Industrial

Source Technology Development Programs (ISTDP10033633) in the Ministry of Knowledge Economy in Korea.

References

1. G. Binnig, H. Rohrer, C. Gerber and E. Weibel, *Appl. Phys. Lett.* **40** (1982) 178.
2. G. Binning, H. Rohrer, C. Gerber and E. Weibel, *Phys. Rev. Lett.* **49** (1982) 57.
3. G. Binnig, H. Rohrer, C. Gerber and E. Weibel, *Physica B & C* **109** (1982) 2075.
4. G. Binnig, H. Rohrer, C. Gerber and E. Weibel, *Phys. Rev. Lett.* **50** (1983) 120.
5. K. D. Jandt, *Mater. Sci. Eng. R* **21** (1998) 221.
6. F. Anariba, *Fabrication and Electrical Characterization of Molecular Junctions: A Robust Platform for Electron Transport Studies in Molecular Electronics* (VDM Verlag, 2010).
7. A. Lewis, M. Isaacson, A. Harootunian and A. Muray, *Ultramicroscopy* **13** (1984) 227.
8. M. Edidin, *Traffic* **2** (2001) 797.
9. W. J. Kaiser and L. D. Bell, *Phys. Rev. Lett.* **60** (1988) 1406.
10. C. D. Frisbie, L. F. Rozsnyai, A. Noy, M. S. Wrighton and C. M. Lieber, *Science* **265** (1994) 2071.
11. L. Zhang, T. Sakai, N. Sakuma, T. Ono and K. Nakayama, *Appl. Phys. Lett.* **75** (1999) 3527.
12. S. R. Higgins and R. J. Hamers, *J. Vac. Sci. Technol. B* **14** (1996) 1360.
13. J. M. R. Weaver and D. W. Abraham, *J. Vac. Sci. Technol. B* **9** (1991) 1559.
14. U. Hartmann, *J. Appl. Phys.* **64** (1988) 1561.
15. A. M. Mansanares, T. Velinov, Z. Bozoki, D. Fournier and A. C. Boccara, *J. Appl. Phys.* **75** (1994) 3344.
16. A. J. Bard, F. R. F. Fan, J. Kwak and O. Lev, *Anal. Chem.* **61** (1989) 132.
17. J. R. Matey and J. Blanc, *J. Appl. Phys.* **57** (1985) 1437.
18. P. K. Hansma, B. Drake, O. Marti, S. A. Gould and C. B. Prater, *Science* **243** (1989) 641.
19. E. Henderson, P. G. Haydon and D. S. Sakaguchi, *Science* **257** (1992) 1944.
20. H. X. You, J. M. Lau, S. Zhang and L. Yu, *Ultramicroscopy* **82** (2000) 297.
21. A. I. Shevchuk, J. Gorelik, S. E. Harding, M. J. Lab, D. Klenerman and Y. E. Korchev, *Biophys. J.* **81** (2001) 1759.
22. S. A. Mann, G. Hoffmann, A. Hengstenberg, W. Schuhmann and I. D. Dietzel, *J. Neurosci. Methods* **116** (2002) 113.
23. P. Novak, C. Li, A. I. Shevchuk, R. Stepanyan, M. Caldwell, S. Hughes, T. G. Smart, J. Gorelik, V. P. Ostanin, M. J. Lab, G. W. Moss, G. I. Frolenkov, D. Klenerman and Y. E. Korchev, *Nat. Methods* **6** (2009) 279.
24. P. Happel and I. D. Dietzel, *J. Nanobiotechnol.* **7** (2009) 7.
25. Y. Takahashi, Y. Murakami, K. Nagamine, H. Shiku, S. Aoyagi, T. Yasukawa, M. Kanzaki and T. Matsue, *Phys. Chem. Chem. Phys.* **12** (2010) 10012.
26. P. Happel, F. Wehner and I. D. Dietzel, in *Modern Research and Educational Topics in Miscroscopy*, eds. A. Mendez-Vilas and J. Diaz, Vol. 2 (Formatex, 2007), p. 968.
27. H. Nitz, J. Kamp and H. Fuchs, *Probe Microsc.* **1** (1998) 187.
28. M. A. Edwards, C. G. Williams, A. L. Whitworth and P. R. Unwin, *Anal. Chem.* **81** (2009) 4482.
29. D. Pastre, H. Iwamoto, J. Liu, G. Szabo and Z. Shao, *Ultramicroscopy* **90** (2001) 13.
30. C. C. Chen and L. A. Baker, *Analyst* **136** (2011) 90.
31. J. Rheinlaender and T. E. Schaffer, *J. Appl. Phys.* **105** (2009) 094905.

32. Y. E. Korchev, M. Milovanovic, C. L. Bashford, D. C. Bennett, E. V. Sviderskaya, I. Vodyanoy and M. J. Lab, *J. Microsc.* **188** (1997) 17.
33. Y. E. Korchev, C. L. Bashford, M. Milovanovic, I. Vodyanoy and M. J. Lab, *Biophys. J.* **73** (1997) 653.
34. J. Gorelik, N. N. Ali, S. H. Sheikh Abdul Kadir, M. Lab, P. Stojkovic, L. Armstrong, E. V. Sviderskaya, Y. A. Negulyaev, D. Klenerman, D. C. Bennett, M. Lako, S. E. Harding, M. Stojkovic and Y. E. Korchev, *Tissue Eng: Part C Methods* **14** (2008) 311.
35. S. E. Harding, N. N. Ali, M. Brito-Martins and J. Gorelik, *Pharmacology & Therapeutics* **113** (2007) 341.
36. M. Miragoli, A. Moshkov, P. Novak, A. Shevchuk, V. O. Nikolaev, I. El-Hamamsy, C. M. Potter, P. Wright, S. H. Kadir, A. R. Lyon, J. A. Mitchell, A. H. Chester, D. Klenerman, M. J. Lab, Y. E. Korchev, S. E. Harding and J. Gorelik, *J. R. Soc. Interface* **8** (2011) 913.
37. J. Rheinlaender, N. A. Geisse, R. Proksch and T. E. Schaffer, *Langmuir* **27** (2011) 697.
38. J. Gorelik, Y. Zhang, A. I. Shevchuk, G. I. Frolenkov, D. Sanchez, M. J. Lab, I. Vodyanoy, C. R. Edwards, D. Klenerman and Y. E. Korchev, *Mol. Cell Endocrinol.* **217** (2004) 101.
39. A. I. Shevchuk, G. I. Frolenkov, D. Sanchez, P. S. James, N. Freedman, M. J. Lab, R. Jones, D. Klenerman and Y. E. Korchev, *Angew. Chem. Int. Ed. Engl.* **45** (2006) 2212.
40. J. Gorelik, A. I. Shevchuk, G. I. Frolenkov, I. A. Diakonov, M. J. Lab, C. J. Kros, G. P. Richardson, I. Vodyanoy, C. R. Edwards, D. Klenerman and Y. E. Korchev, *Proc. Natl. Acad. Sci.* **100** (2003) 5819.
41. Y. Zhang, J. Gorelik, D. Sanchez, A. Shevchuk, M. Lab, I. Vodyanoy, D. Klenerman, C. Edwards and Y. Korchev, *Kidney Int.* **68** (2005) 1071.
42. Y. E. Korchev, Y. A. Negulyaev, C. R. Edwards, I. Vodyanoy and M. J. Lab, *Nat. Cell Biol.* **2** (2000) 616.
43. P. Happel, G. Hoffmann, S. A. Mann and I. D. Dietzel, *J. Microsc.* **212** (2003) 144.
44. J. Gorelik, L. Q. Yang, Y. Zhang, M. Lab, Y. Korchev and S. E. Harding, *Cardiovasc. Res.* **72** (2006) 422.
45. H. Duclohier, *Biochem. Biophys. Res. Commun.* **334** (2005) 1135.
46. W. Shin and K. D. Gillis, *Biophys. J.* **91** (2006) L63.
47. C. Kung, *Nature* **436** (2005) 647.
48. H. Cho, J. Shin, C. Y. Shin, S.-Y. Lee and U. Oh, *J. Neurosci.* **22** (2002) 1238.
49. X. Su, R. E. Wachtel and G. F. Gebhart, *J. Neurophysiol.* **84** (2000) 836.
50. A. Ghazi, C. Berrier, B. Ajouz and M. Besnard, *Biochimie* **80** (1998) 357.
51. D. Sanchez, U. Anand, J. Gorelik, C. D. Benham, C. Bountra, M. Lab, D. Klenerman, R. Birch, P. Anand and Y. Korchev, *J. Neurosci. Methods* **159** (2007) 26.
52. D. Sanchez, N. Johnson, C. Li, P. Novak, J. Rheinlaender, Y. Zhang, U. Anand, P. Anand, J. Gorelik, G. I. Frolenkov, C. Benham, M. Lab, V. P. Ostanin, T. E. Schaffer, D. Klenerman and Y. E. Korchev, *Biophys. J.* **95** (2008) 3017.
53. M. Pellegrino, P. Orsini and F. De Gregorio, *Neurosci. Res.* **64** (2009) 290.
54. M. Pellegrino, P. Orsini, M. Pellegrini, P. Baschieri, F. Dinelli, D. Petracchi, E. Tognoni and C. Ascoli, *Neurosci. Res.* **69** (2011) 234.
55. L. Ying, A. Bruckbauer, A. M. Rothery, Y. E. Korchev and D. Klenerman, *Anal. Chem.* **74** (2002) 1380.
56. L. Ying, S. S. White, A. Bruckbauer, L. Meadows, Y. E. Korchev and D. Klenerman, *Biophys. J.* **86** (2004) 1018.

57. L. Ying, A. Bruckbauer, D. Zhou, J. Gorelik, A. Shevchuk, M. Lab, Y. Korchev and D. Klenerman, *Phys. Chem. Chem. Phys.* **7** (2005) 2859.
58. A. Bruckbauer, L. Ying, A. M. Rothery, D. Zhou, A. I. Shevchuk, C. Abell, Y. E. Korchev and D. Klenerman, *J. Am. Chem. Soc.* **124** (2002) 8810.
59. A. Bruckbauer, D. Zhou, L. Ying, Y. E. Korchev, C. Abell and D. Klenerman, *J. Am. Chem. Soc.* **125** (2003) 9834.
60. A. Bruckbauer, D. J. Zhou, L. M. Ying, C. Abell and D. Klenerman, *Nano Lett.* **4** (2004) 1859.
61. K. T. Rodolfa, A. Bruckbauer, D. Zhou, Y. E. Korchev and D. Klenerman, *Angew. Chem. Int. Ed. Engl.* **44** (2005) 6854.
62. K. T. Rodolfa, A. Bruckbauer, D. Zhou, A. I. Schevchuk, Y. E. Korchev and D. Klenerman, *Nano Lett.* **6** (2006) 252.
63. A. Bruckbauer, P. James, D. Zhou, J. W. Yoon, D. Excell, Y. Korchev, R. Jones and D. Klenerman, *Biophys. J.* **93** (2007) 3120.
64. K. L. Christman, V. D. Enriquez-Rios and H. D. Maynard, *Soft Matter* **2** (2006) 928.
65. E. Neher and B. Sakmann, *Nature* **260** (1976) 799.
66. E. Neher, B. Sakmann and J. H. Steinbach, *Pflugers Arch.* **375** (1978) 219.
67. O. P. Hamill, A. Marty, E. Neher, B. Sakmann and F. J. Sigworth, *Pflugers Arch.* **391** (1981) 85.
68. Y. Gu, J. Gorelik, H. A. Spohr, A. Shevchuk, M. J. Lab, S. E. Harding, I. Vodyanoy, D. Klenerman and Y. E. Korchev, *FASEB J.* **16** (2002) 748.
69. J. Gorelik, Y. Gu, H. A. Spohr, A. I. Shevchuk, M. J. Lab, S. E. Harding, C. R. Edwards, M. Whitaker, G. W. Moss, D. C. Benton, D. Sanchez, A. Darszon, I. Vodyanoy, D. Klenerman and Y. E. Korchev, *Biophys. J.* **83** (2002) 3296.
70. A. K. Dutta, Y. E. Korchev, A. I. Shevchuk, S. Hayashi, Y. Okada and R. Z. Sabirov, *Biophys. J.* **94** (2008) 1646.
71. J. Gorelik, A. Shevchuk, M. Ramalho, M. Elliott, C. Lei, C. F. Higgins, M. J. Lab, D. Klenerman, N. Krauzewicz and Y. Korchev, *Proc. Natl. Acad. Sci.* **99** (2002) 16018.
72. A. I. Shevchuk, P. Hobson, M. J. Lab, D. Klenerman, N. Krauzewicz and Y. E. Korchev, *Pflugers Arch.* **456** (2008) 227.
73. A. I. Shevchuk, P. Hobson, M. J. Lab, D. Klenerman, N. Krauzewicz and Y. E. Korchev, *Biophys. J.* **94** (2008) 4089.
74. Y. E. Korchev, M. Raval, M. J. Lab, J. Gorelik, C. R. Edwards, T. Rayment and D. Klenerman, *Biophys. J.* **78** (2000) 2675.
75. A. Mannelquist, H. Iwamoto, G. Szabo and Z. F. Shao, *Appl. Phys. Lett.* **78** (2001) 2076.
76. A. Mannelquist, H. Iwamoto, G. Szabo and Z. Shao, *J. Microsc.* **205** (2002) 53.
77. A. M. Rothery, J. Gorelik, A. Bruckbauer, W. Yu, Y. E. Korchev and D. Klenerman, *J. Microsc.* **209** (2003) 94.
78. A. J. Bard, F. R. Fan, D. T. Pierce, P. R. Unwin, D. O. Wipf and F. Zhou, *Science* **254** (1991) 68.
79. C. Wei, A. J. Bard, G. Nagy and K. Toth, *Anal. Chem.* **67** (1995) 1346.
80. D. A. Walsh, J. L. Fernandez, J. Mauzeroll and A. J. Bard, *Anal. Chem.* **77** (2005) 5182.
81. Y. Takahashi, A. I. Shevchuk, P. Novak, Y. Murakami, H. Shiku, Y. E. Korchev and T. Matsue, *J. Am. Chem. Soc.* **132** (2010) 10118.
82. D. J. Comstock, J. W. Elam, M. J. Pellin and M. C. Hersam, *Anal. Chem.* **82** (2010) 1270.
83. G. B. Kolata, *Science* **188** (1975) 819.
84. K. R. Porter, G. J. Todaro and V. Fonte, *J. Cell Biol.* **59** (1973) 633.
85. M. C. Willingham and I. Pastan, *Proc. Natl. Acad. Sci.* **72** (1975) 1263.